



Dragonfly: Multi-Resolution Zoom Supercharges Large Visual-Language Model

Kezhen Chen^{1*} Rahul Thapa^{1,2*}
Rahul Chalamala^{1,3} Ben Athiwaratkun¹ Shuaiwen Leon Song¹ James Zou^{1,2}
¹Together AI ²Stanford University ³Caltech
{kezhen, rahul, ben, leon}@together.ai
{rthapa84, jamesz}@stanford.edu

Abstract

Recent advances in large multimodal models (LMMs) suggest that higher image resolution enhances the fine-grained understanding of image details, crucial for tasks such as visual commonsense reasoning and analyzing biomedical images. However, increasing input resolution poses two main challenges: 1) It extends the context length required by the language model, leading to inefficiencies and hitting the model’s context limit; 2) It increases the complexity of visual features, necessitating more training data or more complex architecture. We introduce Dragonfly, a new LMM architecture that enhances fine-grained visual understanding and reasoning about image regions to address these challenges. Dragonfly employs two key strategies: multi-resolution visual encoding and zoom-in patch selection. These strategies allow the model to process high-resolution images efficiently while maintaining reasonable context length. Our experiments on eight popular benchmarks demonstrate that Dragonfly achieves competitive or better performance compared to other architectures, highlighting the effectiveness of our design. Additionally, we finetuned Dragonfly on biomedical instructions, achieving state-of-the-art results on multiple biomedical tasks requiring fine-grained visual understanding, including 92.3% accuracy on the Path-VQA dataset (compared to 83.3% for Med-Gemini) and the highest reported results on biomedical image captioning. To support model training, we curated a visual instruction-tuning dataset with 5.5 million image-instruction samples in the general domain and 1.4 million samples in the biomedical domain. We also conducted ablation studies to characterize the impact of various architectural designs and image resolutions, providing insights for future research on visual instruction alignment. The codebase and model are available at <https://github.com/togethercomputer/Dragonfly>.

1 Introduction

Recent progress in large multimodal models (LMMs) has underscored the importance of effectively integrating visual information into large language models (LLMs). Impressive performance is achieved through sophisticated visual encoding strategies, which are pivotal in projecting complex real-world visual information into the latent space of LLMs. One of the prominent architectures in LMMs is vision instruction alignment, which encodes image inputs into patch-level tokens using a pretrained image encoder. Then, these visual tokens are projected into the latent space of an LLM through visual instruction-tuning (Liu et al., 2023b,a; Yang et al., 2023; Li et al., 2023; Xu et al., 2023; McKinzie et al., 2024; Laurençon et al., 2024; You et al., 2023; Zhang et al., 2024).

*Equal contribution.

Despite these advancements, most existing LMMs process images at a fixed aspect ratio and low resolution, causing high-resolution images to be downsampled before being passed to the model. The downsampling often results in shape distortion and the loss of fine details (Xu et al., 2023). However, many visual reasoning or biomedical tasks require models to capture fine-grained details in image regions. Recent studies suggest that encoding higher resolution images could provide more detailed information, thereby improving fine-grained visual understanding (McKinzie et al., 2024; Laurençon et al., 2024; Liu et al., 2023a; Zhang et al., 2024). One strategy is using better image encoders trained on high-resolution images. For example, Liu et al. (2023a) and Laurençon et al. (2024) replaced the low-resolution image encoder trained on 224x224 images with high-resolution image encoders trained on 336x336 or 384x384 images, resulting in performance improvements on multiple benchmarks. Xu et al. (2023) and Zhang et al. (2024) further enhance the vision encoding by resizing original images into two different resolutions to encode both abstract and detailed information.

However, existing methods face two key challenges when encoding high-resolution images: filling more of the context window leads to lower model efficiency, and higher resolutions may have more redundant patches. An image with a resolution of 336x336 is encoded into 576 visual tokens in the architecture from Liu et al. (2023a). In the biomedical domain, images are much higher resolution and may require more visual tokens to capture detailed information. Also, more patches in higher-resolution encoding may be irrelevant to the given query, which leads to more complexity and noise. Some tasks may only require focus on high-resolution regions of the images.

To address these challenges, we introduce a new LMM architecture, Dragonfly, focusing on fine-grained understanding and reasoning on image regions while maintaining high efficiency. Dragonfly incorporates two key techniques: multi-resolution visual encoding and zoom-in patch selection. Inspired by multiple works (Liu et al., 2023a; Xu et al., 2023; Laurençon et al., 2024), we encode multi-resolution information of the images by adjusting the original input image into three distinct resolutions—low, medium, and high—to capture information at multiple granularities. Dragonfly also employs a zoom-in patch selection method to enhance fine-grained understanding of image regions by selecting the most informative visual tokens from high-resolution images. With this approach, Dragonfly focuses on relevant high-resolution regions of the image instead of using all the visual tokens of high-resolution images. This new technique enables Dragonfly to demonstrate its fine-grained processing capabilities on multiple popular benchmarks and biomedical tasks. Furthermore, we conducted comprehensive ablation studies focusing on patch selection strategies and image resolution. To support these studies, we curated a visual instruction-tuning dataset with 5.5 million general-domain and 1.4 million biomedical-domain samples. The model, codebase, and training data will be available upon acceptance.

In summary, **our contributions** are as follows:

- We introduce Dragonfly, an innovative LMM architecture that utilizes multi-resolution visual encoding and zoom-in patch selection, enabling Dragonfly to process fine-grained image details efficiently. Trained on our curated dataset of 5.5 million image-instruction samples, Dragonfly outperforms the baselines on five popular benchmarks, providing evidence of the architecture’s effectiveness.
- We demonstrate our model’s understanding and reasoning capabilities on biomedical tasks, which often require a fine-grained understanding of high-resolution image regions. By finetuning our general-domain model on a biomedical instruction-tuning dataset with 1.4 million biomedical image-text pairs, Dragonfly-Med, our biomedical version of the model, achieves state-of-the-art or competitive performance on multiple biomedical benchmarks, including visual question answering (VQA), image captioning, and radiology report generation. For example, Dragonfly-Med achieves 92.3% accuracy on the Path-VQA dataset (He et al., 2020), a 58.8 CIDEr score on the IU X-Ray dataset (Demner-Fushman et al., 2016), and a 179.9 CIDEr score on the Peir Gross dataset (Jing et al., 2017).
- We conducted extensive ablation studies to investigate the impacts of patch selection strategies and image resolution. These studies enhance our understanding of the factors influencing model training and provide valuable insights that inform our design choices.

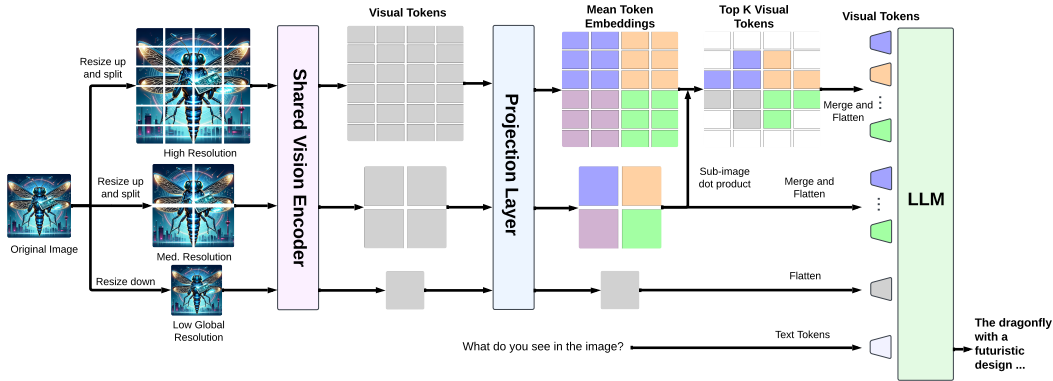


Figure 1: Overview of the proposed Dragonfly model architecture. The original image is resized into low, medium, and high resolutions. The medium and high-resolution images are divided into sub-images, aligning with the encoder’s training resolution. All sub-images pass through a shared vision encoder to produce visual tokens. The projection layer maps the visual tokens to the language space, and the mean of these projected token embeddings serves as the summary token embeddings. For each mid-resolution embedding, we select the top 3 high-resolution sub-images from the corresponding regions based on the dot product similarity of the projected tokens, resulting in 12 non-overlapping high-resolution sub-images. Finally, visual tokens from the top high-resolution sub-images, along with all tokens from low and mid-resolution images, are flattened and passed to the LLM.

2 Related Work

The advancement of LLMs has significantly impacted vision-language research by facilitating the integration of visual representations into language models, allowing LLMs to utilize their extensive language knowledge while incorporating newly emerging visual capabilities (Wei et al., 2022). Visual feature alignment is one of the predominant methods to introduce multimodal capabilities into LLMs. This approach maps visual embeddings into the language space, effectively merging vision and language through visual instruction-tuning (Liu et al., 2023b,a; Dai et al., 2023; Yang et al., 2023; Li et al., 2023; Xu et al., 2023; McKinzie et al., 2024; Laurençon et al., 2024; You et al., 2023; Awadalla et al., 2023). For instance, Liu et al. (2023b) employs a fully connected layer to project image embeddings generated by a pretrained CLIP encoder (Radford et al., 2021) into the large language model’s embedding space. Similarly, Awadalla et al. (2023) and Li et al. (2023) adopt the Flamingo framework Alayrac et al. (2022), utilizing a Perceiver Resampler with cross-attention (Jaegle et al., 2022) to integrate visual tokens into the language domain. Models utilizing embedding alignment methods have demonstrated considerable success across various benchmarks, showcasing the efficacy of embedding alignment in vision-language tasks. However, a limitation among these models is their reliance on downscaling input images to a fixed low resolution, which sacrifices visual detail. McKinzie et al. (2024) and Laurençon et al. (2024) have provided evidence that higher-resolution visual inputs can enhance the model performance and reasoning on fine-grained visual contents. Liu et al. (2023a) and Xu et al. (2023) have refined this approach by segmenting native-resolution images into smaller, variable-sized slices that closely align with the traditional pretraining configurations of image encoders. Recently, Fuyu (AdeptAI, 2023), a decoder-only model that supports arbitrary image resolutions, has been used as an alternative to circumvent the drawbacks of downscaling. By linearly projecting image patches into the transformer’s first layer, Fuyu treats the sequence of image patches similar to text tokens AdeptAI (2023). Despite these improvements, the contextual constraints of LLMs still pose challenges. These methods often require excessive visual tokens to encode higher-resolution images, leading to inefficiencies. In contrast, Dragonfly applies a zoom-in patch selection method, choosing a subset of visual tokens from high-resolution images to achieve more efficient processing while focusing on regional fine-grained details. Unlike McKinzie et al. (2024) and Laurençon et al. (2024), our paper focuses only on the visual instruction-tuning stage, aiming to refine and optimize the design of the Dragonfly architecture.

Advancements in LLMs and LMMs have also significantly propelled the development of biomedical vision-language models, integrating medical imaging, literature, and clinical notes. Notable examples

include BiomedGPT (Zhang et al., 2023a), a multi-task biomedical foundation model that combines language modeling and masked image infilling objectives. Similarly, LLaVA-Med (Li et al., 2024a) leverages PubMed and GPT-4 to curate a multimodal instruction-following dataset and finetuning a LLaVA model. Additionally, general-purpose LLMs have been adapted for biomedical applications, as seen in Med-PaLM (Tu et al., 2024), Med-Flamingo (Moor et al., 2023), and Med-Gemini (Saab et al., 2024). These models highlight the potential of leveraging LMMs to address specialized biomedical challenges. Biomedical tasks require models with strong and fine-grained understanding and reasoning capabilities for image regions. For example, identifying a condition might depend on analyzing a specific area of chest X-ray. In this paper, we evaluate the fine-grained image understanding of Dragonfly architecture by finetuning it on biomedical data. With 1.4 million high-quality biomedical visual instruction pairs, our model achieves state-of-the-art or competitive performance on multiple biomedical tasks, all while using a smaller backbone than other baselines.

3 Multi-resolution Zoom Architecture for Dragonfly

We introduce Dragonfly, an innovative LMM architecture that uniquely incorporates multi-resolution visual encoding and zoom-in patch selection to enhance the visual understanding of regional details. Figure 1 illustrates the Dragonfly architecture, which consists of an image encoder E , a projection layer P , and an LLM L . Given a pair of an image I and a text instruction T , the image encoder E encodes the image into n visual tokens $\{v_i\}_{i=1}^n$, and the projection layer maps the visual tokens to the language space to construct the input tokens $\{t_i\}_{i=1}^n$. Then, the projected visual and text tokens are concatenated to construct the sequence of embeddings passed to the LLM. This section presents the technical details of multi-resolution visual encoding and zoom-in patch selection.

3.1 Multi-resolution Visual Encoding

Dragonfly leverages multi-resolution visual encoding through a shared image encoder E trained on a fixed image resolution: $R \times R$. Drawing on strategies from prior works Liu et al. (2023a); Xu et al. (2023), Dragonfly handles larger images by dividing them into multiple sub-images, each matching the encoder’s training resolution. Specifically, given an image I , Dragonfly resizes it into three distinct resolutions: a low-resolution image I^l sized $R \times R$, a medium-resolution image I^m sized $x^m R \times y^m R$, and a high-resolution image I^h sized $x^h R \times y^h R$. The medium and high-resolution images are segmented into two sets of sub-images, $\{I_i^m\}_{i=1}^{x^m \times y^m}$ and $\{I_j^h\}_{j=1}^{x^h \times y^h}$, respectively, aligning with the training resolution $R \times R$ of the encoder E .

The image encoder E encodes each sub-image into a series of visual tokens $\{v_1 \dots v_n\}$. These tokens from various sub-images are then projected into the latent space of the language model via the projection layer P , and a sequence of projected tokens $\{t_1 \dots t_n\}$ are generated. The projected tokens from different sets of sub-images are concatenated to form a comprehensive representation of the image and are used for LLM understanding. However, the number of sub-images, particularly from the high-resolution set, can be extensive. As previously mentioned, utilizing all these sub-images could lead to a longer context length and introduce noisy features during training. Dragonfly adopts a selective approach, using a novel zoom-in patch selection method to choose only a subset of sub-images that contain richer visual information. Thus, Dragonfly enhances the fine-grained understanding of image regions while keeping efficiency. The following section details the mechanics of the zoom-in patch selection method.

3.2 Zoom-in Patch Selection

Dragonfly employs a multi-resolution visual encoding strategy to efficiently process images while capturing both abstract and fine-grained visual information. The model processes all the visual tokens encoded for low and medium-resolution images. Even when segmented into smaller sub-images, these images do not produce excessive visual tokens and mainly provide a more abstract representation of the visual content. However, the sub-images from the high-resolution set are treated differently due to their potential to generate many sub-images, some of which may be redundant. To address this, Dragonfly introduces the zoom-in patch selection method only to select a subset of high-resolution sub-images, effectively reducing redundancy. Each high-resolution sub-image is a magnified view of a specific area of the original image. We only identify and retain patches that correspond semantically

to the medium-resolution sub-images. This targeted selection helps enrich the image representation with detailed information on critical content areas and drop redundant sub-images.

To facilitate this selection, we construct a summary embedding a for each sub-image in both the *medium-resolution* and *high-resolution* sets. For the medium-resolution sub-images, the summary embedding is denoted as a^m , and for the high-resolution sub-images, as a^h . We compute the mean vector of the projected sequence of tokens $\{t_1 \dots t_n\}$ from the projection layer P as the summary embedding. As the projection layer P projects visual tokens $\{v_1 \dots v_n\}$ to the tokens $\{t_1 \dots t_n\}$ in the latent space of LLMs, the summary embedding a is a vector that encapsulates the overall semantic information from the language space of the corresponding sub-image.

Given a summary embedding a_i^m for a medium-resolution sub-image I_i^m , Dragonfly identifies a set of k most similar high-resolution sub-images $I_{i_1}^h \dots I_{i_k}^h$ from the high-resolution set of the corresponding region. We use the a_i^m to match the summary embeddings $\{a_{i_j}^h\}_{j=1}^k$ from the high-resolution set of the corresponding region by calculating their dot-product embedding similarity. Note that the number of sub-images of the high-resolution set of the corresponding region is $s = \frac{x^h \times y^h}{x^m \times y^m}$. The corresponding high-resolution sub-images, identified by their matched embeddings, are then integrated into the final sequence of tokens for the LLM. This selective process effectively minimizes redundancy while concentrating on the most visually significant parts of the image. The mathematical representation of this process is outlined as follows:

$$a_i^m = \frac{1}{N} \sum_{i=1}^N P(v_i^m) \quad a_j^h = \frac{1}{N} \sum_{j=1}^N P(v_j^h) \quad (1)$$

$$\{I_{i_j}^h\}_{j=1}^k = \operatorname{argmax}_{i_1 \dots i_k} (\operatorname{sim}(a_i^m, a_j^h)), a_i^m \in \{a^m\}_{i=1}^{x^m \times y^m}, a_j^h \in \{a^h\}_{j=s \times i}^{s \times (i+1)} \quad (2)$$

$$V = \operatorname{Concat}(\{t_1^l, \dots, t_n^l\}, \{t_{i_1}^m, \dots, t_{i_n}^m\}_{i=1}^{x^m \times y^m}, \{\{t_{i_j}^h\}_{j=1}^k\}_{i=1}^{x^m \times y^m}) \quad (3)$$

Following the zoom-in patch selection, the projected tokens $\{t_1 \dots t_n\}$ from the resized low-resolution image, the sub-images of the medium-resolution image, and the selected sub-images of the high-resolution are concatenated to form the latent embeddings $\{T^V\}$ of the original image I for the LLM. Dragonfly merges the processed tokens for the images, $\{T^V\}$, with the text tokens $\{T^T\}$ generated by the LLM’s embedding layer and forwards them to the LLM to produce the final output.

4 Experiments

To evaluate the effectiveness of our architecture, we construct various baselines with different settings and conduct experiments on multiple popular multimodal benchmarks. In this section, we first introduce our implementation. Then, we describe our experiment results on general domain benchmarks. Finally, we evaluate Dragonfly’s fine-grained understanding of biomedical tasks.

4.1 Implementation

We adopt the popular two-stage visual instruction-tuning framework introduced in Liu et al. (2023b). In the first stage, the LLM and the vision encoder are frozen, allowing only the projection layer to be trained. This stage enables the projection layer to learn how to map vision tokens effectively into the language space while preserving the established language alignment of the LLM. The entire model undergoes finetuning in the subsequent stage using a high-quality visual instruction-tuning dataset. This step is crucial as it enhances the alignment of visual features with the language space, optimizing the model’s overall performance in handling vision-language tasks. Dragonfly uses Llama3-8B-chat (Meta AI, 2024) as the backbone and CLIP-vit-base-patch32 (Radford et al., 2021) as the image encoder. Although there are many visual encoders with higher resolution and better performance, we chose this encoder to reduce the effects of the visual encoder and better understand our model architecture. Could Dragonfly achieve competitive performance compared with other LLMs with better visual encoders? For both stages, the low resolution corresponds to 224x224 to match the resolution of the image encoder. We apply the same any-resolution method from Xu et al. (2023) to

Table 1: Comparison results between Dragonfly and baselines on the eight benchmarks. The best results are in bold font, and the second-best performances are underlined. AI2D and ScienceQA are mainly focused on commonsense reasoning. ChartQA evaluates the chart understanding capability. MMMU and MMVet evaluate the unified LMM capabilities. Pope and Hallucination-Bench evaluates the hallucination of the object or image details. COCO tests the image captioning.

Benchmark	Metric	Baseline-1	Baseline-2	Baseline-3	Ours
AI2D	Acc	58.1	49.48	<u>60.81</u>	62.37
ScienceQA	Acc	65.79	61.63	<u>70.17</u>	73.14
ChartQA	Relaxed Acc	28.6	46.24	<u>45.92</u>	37.43
MMMU-val	Acc	33.4	35.1	36.6	<u>36.2</u>
MMVet	GPT-Eval-Avg	28.8	<u>30.2</u>	29.7	31.7
Pope-f1	F1 Score	<u>81.81</u>	77.06	71.59	83.23
COCO-val	CIDEr	89.02	<u>91.20</u>	86.84	94.07
Hallucination-Bench	Acc	<u>41.9</u>	41.12	44.11	41.37

segment the image into multiple sub-images. The any-resolution chooses the resolution from a set of possible resolution grids closest to the original image aspect ratio. The medium resolution uses a set of possible grids $\{(2,2),(1,4),(4,1)\}$, resulting in the four sub-images. In the current implementation, the high resolution uses the $\{(6,4), (4,6), (3,8), (8,3)\}$ grids, resulting in 24 sub-images, and we select 12 sub-images from the 24 sub-images in the zoom-in patch selection. For the first training stage, the model is trained on LLaVA-Pretrain (Liu et al., 2023b) with 558K image-text pairs using the global batch size 64 with the learning rate $2e-5$. The global batch size in the second training stage is 16, and the learning rate is $2e-6$. Both stages only train the model one epoch on the training dataset. To support the model training and experiments, we curated a data mixture with 5,580,560 image-instruction samples from multiple sources, containing detailed image descriptions, complicated reasoning, and question-answering tasks. Besides the dataset for the general domain tasks, we also collect 1.4 million visual instruction samples for the biomedical domain to evaluate the domain adaption capability of our model. Further details about the instruction-tuning dataset are provided in Appendix sections A and C. The training utilized 8 NVIDIA H100 GPUs with DeepSpeed ZeRO stage 1 and lasted approximately 73 hours.

4.2 Results

We construct several baselines to evaluate the effectiveness of the Dragonfly architecture. For a fair comparison, all baselines utilize the same image encoder and LLM backbone and are trained for 100,000 steps in training stage 2 on the same data mixture using the same random seed. We use LLaVA-1.6 (Liu et al., 2023a) as the baseline architecture because this framework resizes the image into two distinct resolutions—low and medium—to capture different levels of visual information, aligning with the goals of Dragonfly. The first baseline (Baseline-1) utilizes grid settings of (1, 1) for low resolution and $\{(2, 2), (1, 4), (4, 1)\}$ for medium resolution, resulting in a total of five sub-images. The second baseline (Baseline-2) adopts grid settings of (1, 1) for low resolution and $\{(4, 4), (2, 8), (8, 2)\}$ for medium resolution, resulting in 17 sub-images. While Dragonfly uses higher image resolutions and zoom-in patch selection, it encodes the image with the same number of sub-images as Baseline-2. The final baseline (Baseline-3) uses grid settings of (1, 1) for low resolution and $\{(6, 4), (4, 6), (3, 8), (8, 3)\}$ for medium resolution, matching the highest resolution of Dragonfly. However, without the zoom-in patch selection, Baseline-3 generates 25 sub-images. We assess the baselines and our model across eight popular benchmarks covering commonsense reasoning QA, image captioning, chart understanding, and hallucination detection. Table 1 shows the comparison results on these eight benchmarks, with detailed descriptions of each benchmark provided in Appendix Section B.

Based on the results, Dragonfly outperforms all the baselines in five benchmarks and achieves competitive performance in the other three. The results demonstrate the effectiveness of our architecture, particularly in image understanding and reasoning. Additionally, we note two intriguing observations from the experiment. First, although Baseline-3 utilizes all sub-images at the same resolution as Dragonfly, its performance does not significantly exceed that of Dragonfly or even Baseline-2, suggesting that some high-resolution sub-images might introduce excessive complexity and noise. A more comprehensive approach, such as zoom-in patch selection, may be required to

Table 2: Comparison between Dragonfly and existing LMMs. Given the limited space, we only present a subset of popular LMMs with a LLM backbone between 7B - 13B parameters, including InstructBLIP(Dai et al., 2023), Qwen-VL(Bai et al., 2023), VILA(Lin et al., 2024), LLaVA-v1.5(Liu et al., 2023b), LLaVA-NeXT(Liu et al., 2023a), MM1(McKinzie et al., 2024), Idefics2(Laurençon et al., 2024). The LLM backbone, visual encoder, training data, and architecture significantly influence the results. Dragonfly achieves promising performance on AI2D, ScienceQA, MMMU-val, and POPE. The model has lower performance on ChartQA as our training dataset has limited chart data. Note that the results for LLaVA-series models are reproduced using the evaluation code, and other LMMs’ results are reported from their technical papers or reports.

Model	Backbone	AI2D	ScienceQA	ChartQA	MMMU-val	MMVet	POPE	COCO-Cap
InstructBLIP	Vicuna-7B	-	60.5	-	-	26.2	-	-
Qwen-VL-Chat	Qwen-7B	62.3	68.2	65.7	35.9	-	-	-
LLaVA-v1.5	Vicuna-7B	54.8	70.4	18.2	35.3	30.5	85.9	-
VILA	Llama2-7B	-	68.2	-	-	34.9	85.5	-
LLaVA-NeXT	Mistral-7B	60.8	72.8	38.8	33.4	44.8	86.7	109.2
LLaVA-NeXT	Vicuna-7B	66.6	70.1	54.8	35.8	43.9	86.5	99.9
LLaVA-NeXT	Llama3-8B	60.9	73.3	-	36.8	-	86.4	-
MM1	MM1-7B	-	72.6	-	37.0	42.1	86.6	-
Idefics2	Mistral-7B	-	-	-	43.0	-	-	116.0
InstructBLIP	Vicuna-13B	-	63.1	-	-	-	78.9	-
LLaVA-v1.5	Vicuna-13B	59.4	74.9	18.2	34.8	35.2	85.9	115.6
VILA	Llama2-13B	-	73.7	-	-	38.8	84.2	-
LLaVA-NeXT	Vicuna-13B	-	73.6	-	36.2	48.8	86.2	-
Dragonfly (Ours)	Llama3-8B	63.6	80.5	29.9	37.8	35.9	91.2	95.8

enhance visual feature alignment. Second, Dragonfly underperforms compared to other baselines on tasks that require OCR or chart understanding. These tasks typically demand visual information from the entire image, and zoom-in patch selection may accidentally omit crucial sub-images. To overcome this limitation, exploring adjustments to the drop ratio or employing a more capable visual encoder could be considered in future works. After training Dragonfly on all samples in our processed dataset, Dragonfly achieves performance that is competitive with or superior to off-the-shelf LMMs across multiple benchmarks. Table 2 shows the comparison results between Dragonfly and other LMMs. Many existing models use different image encoders, LLM backbones, and datasets, making comparing results challenging to interpret. Despite only being trained via visual instruction tuning and using a smaller visual encoder than many of the LMMs, Dragonfly still achieved good performance on AI2D (Kembhavi et al., 2016), ScienceQA (Lu et al., 2022), MMMU-val(Xiang et al., 2023), and POPE(Yifan et al., 2023), highlighting the promising potential of its new architecture.

4.3 Biomedical Domain Adaptation

Biomedical tasks require LMMs to capture fine-grained information on image regions, and we hypothesize that this is especially well-suited for Dragonflyarchitecture. Here, we employed a domain adaptation strategy to assess our model’s ability to generalize to the biomedical domain and evaluate its fine-grained image understanding. Starting with a model checkpoint instruction tuned on a general domain dataset, we implemented a three-step training process tailored specifically for the biomedical domain to create Dragonfly-Med.

Stage 1: Vision Encoder Tuning The initial stage involved tuning the vision encoder, a crucial step given the limited exposure of the standard CLIP vision encoder to biomedical images. The training dataset for this phase predominantly consisted of short caption datasets from sources like LLaVA-Med (Li et al. (2024a)), Openpath (Huang et al. (2023a)), and MedICaT (Subramanian et al. (2020)), supplemented by datasets from the general domain LLaVA-Pretrain (Liu et al. (2024)). This phase included approximately 1.16 million image-text pairs, split roughly evenly between the general and biomedical domains. Stage 1 took about 12 hours to train on 8 NVIDIA H100 GPUs.

Stage 2: Comprehensive Model Tuning The second stage involved jointly training the vision encoder, the language model, and the projection layer. We utilized a diverse set of datasets including LLaVA-Med-Instruct (Li et al. (2024a)), MIMIC-III-CXR (Johnson et al. (2019)), Openpath (Huang et al. (2023a)), ROCO (Pelka et al. (2018)), Kaggle DR, and DDR (Li et al. (2019)). Additionally, we incorporated training sets from benchmark datasets such as VQA-RAD (Lau et al. (2018)), SLAKE

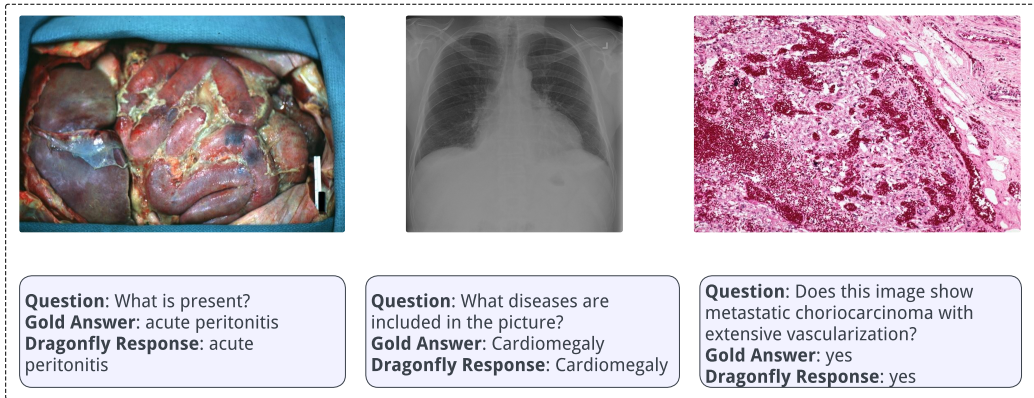


Figure 2: Examples of Biomedical Visual Question Answering (VQA). The figure shows three questions along with their gold standard answers and the corresponding responses from the Dragonfly model.

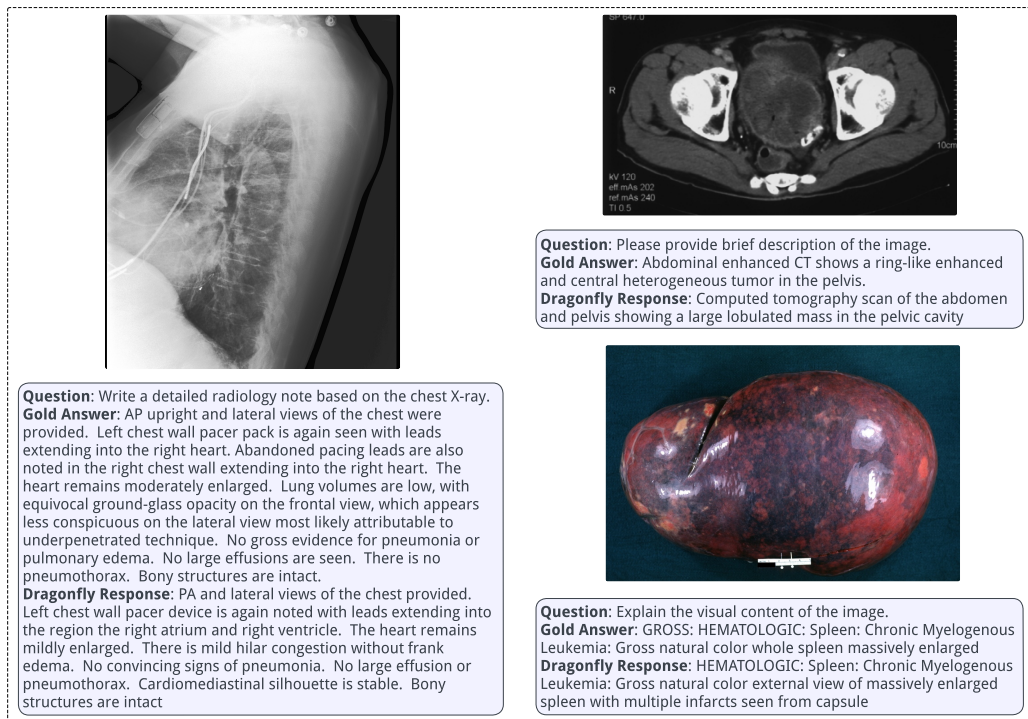


Figure 3: Examples of Biomedical captioning and radiology report generation tasks. The figure shows three questions along with their gold standard answers and the corresponding responses from the Dragonfly model.

(Liu et al. (2021)), Path-VQA (He et al. (2020)), IU X-Ray, and Peir Gross (Demner-Fushman et al. (2016)). The total dataset encompassed 723K image-text pairs, with the composition being approximately 15% from the general domain and 85% from the biomedical domain. We additionally included 70K general domain text-only instruction-tuning dataset. The general domain datasets included Scale up Visual Instruction Tuning (SVIT) Zhao et al. (2023b), ShareGPT4V Chen et al. (2023a), and ArXivCap Li et al. (2024b). Stage 2 took about 9 hours on 8 NVIDIA H100 GPUs.

Stage 3: Supervised Finetuning The final stage involved supervised finetuning using combined training datasets from our benchmark tasks: VQA-RAD, SLAKE, Path-VQA, IU X-Ray, Peir Gross, and subsets of ROCO and MIMIC-CXR. We finetuned a single model end-to-end on this aggregated

training data to optimize performance across all tasks simultaneously. Stage 3 required about an hour of training on 8 NVIDIA H100 GPUs.

The results, as reported in Table 3 and 4, are based on this finetuned model and evaluated against the official held-out test sets of the respective benchmarks (the details of the biomedical benchmarks are described in Appendix Section D). For VQA tasks, we use accuracy and token-level F1 (Tu et al., 2024), while for image captioning and radiology report generation tasks, we use metrics such as ROUGE-L (Lin, 2004), METEOR (Banerjee & Lavie, 2005), and CIDEr (Vedantam et al., 2015). These metrics evaluate the fluency of text, the sequence of content, and the recognition of synonyms and word stems, with CIDEr specifically tailored for assessing text descriptions of images.

Dragonfly-Med achieves competitive performance across multiple benchmarks, outperforming existing state-of-the-art methods on the Path-VQA dataset for both accuracy (closed) and token F1 metrics. Our model attains an accuracy of 90.4% on the SLAKE dataset, which is close to the current state-of-the-art of 91.6%. Notably, Dragonfly-Med outperforms Med-Gemini, a much larger model, on all VQA tasks. On the image captioning task, Dragonfly achieves state-of-the-art or competitive results on several metrics across these datasets. Notably, on the Peir Gross and ROCO datasets, Dragonfly outperforms existing methods on all three metrics: ROUGE-L, METEOR, and CIDEr. Some of the baseline models are much larger than our current implementation. Results on biomedical tasks further support the fine-grained understanding and reasoning capabilities on image regions of Dragonfly architecture. We present a few examples from our evaluation tasks, along with Dragonfly’s responses, in Figures 2 and 3.

Table 3: Biomedical VQA evaluation results.

Dataset	Metric	LLaVA-Med	Med-Gemini	SOTA	Dragonfly-Med (Ours)
VQA-RAD	Acc (closed)	84.2	69.7	87.1 (Tanwani et al., 2022)	77.4
	Token F1	-	50.1	62.1 (Tu et al., 2024)	59.6
SLAKE	Acc (closed)	83.2	84.8	91.6 (Yuan et al., 2023)	90.4
	Token F1	-	75.8	89.3 (Tu et al., 2024)	88.8
Path-VQA	Acc (closed)	91.7	83.3	91.7 (Li et al., 2024a)	92.3
	Token F1	-	58.7	62.7 (Tu et al., 2024)	67.6

Table 4: Medical image captioning and clinical report generation evaluation results. For MIMIC-CXR, we specifically focus on generating the findings section of the radiology report.

Dataset	Metric	BiomedGPT	SOTA	Dragonfly-Med (Ours)
IU X-Ray	ROUGE-L	28.5	44.8 (Zhou et al., 2021)	28.5
	METEOR	12.9	24.2 (Huang et al., 2023b)	29.7
	CIDEr	40.1	43.5 (Wang et al., 2023)	58.8
Peir Gross	ROUGE-L	36.0	36.0 (Zhang et al., 2023a)	40.3
	METEOR	15.4	15.4 (Zhang et al., 2023a)	38.3
	CIDEr	122.7	122.7 (Zhang et al., 2023a)	179.9
ROCO	ROUGE-L	18.2	18.2 (Zhang et al., 2023a)	19.3
	METEOR	7.8	7.8 (Zhang et al., 2023a)	15.1
	CIDEr	24.2	24.2 (Zhang et al., 2023a)	40.1
MIMIC CXR	ROUGE-L	23.8	33.5 (Zhou et al., 2021)	24.2
	METEOR	14.2	19.0 (Zhou et al., 2021)	22.6
	CIDEr	14.7	50.9 (Miura et al., 2020)	47.2

5 Ablation Studies

We conducted several ablation studies to better understand the effects of architecture design and image resolutions. First, we explored two different zoom-in selection strategies, which provided insights for our final design. Second, we investigated the image resolutions in zoom-in patch selection and discovered that different tasks may require different optimal resolutions.

Table 5: Results of the ablation studies on zoom-in selection strategy.

Strategy	AI2D	ScienceQA	ChartQA	MMMU-val	Pope-f1
Global selection	59.45	74.60	33.12	33.4	81.93
Region selection	62.37	73.14	37.43	36.2	83.23

Table 6: Results of the ablation studies on the image resolution for zoom-in patch selection.

Resolution Grid	AI2D	ScienceQA	ChartQA	MMMU-val	Pope-f1
{[4,4],[2,8],[8,2]}	62.24	69.59	38.44	35.8	73.67
{[6,4],[4,6],[3,8],[8,3]}	62.37	73.14	37.43	36.2	83.23
{[6,8],[8,6],[4,12],[12,4]}	58.23	75.43	31.72	37.0	60.69

5.1 Zoom-in Selection Strategy

We evaluate two zoom-in selection strategies to select subsets of the sub-images segmented from the resized high-resolution image. The first strategy, global selection, uses the summary token from each medium-resolution sub-image to directly retrieve 12 sub-images from the entire high-resolution set. This strategy aims to capture the most relevant high-resolution patches based on image-level embedding, focusing on collecting patches containing the original image’s most crucial visual features. The second strategy, region selection, uses the summary token from each medium-resolution sub-image to extract three sub-images from the corresponding high-resolution regions. Unlike global selection, region selection focuses on high-resolution patches from four specific image regions, dividing the medium-resolution image into four sub-images. We evaluate both strategies by training 200K steps on our data mixture. Table 5 shows the results on several benchmarks for the two selection strategies, using the same evaluation metrics as in Table 1. Based on the ablation studies, region selection slightly outperforms global selection, although performance varies across different tasks. In our final implementation, we opted for the region selection strategy because it surpasses global selection in more benchmarks.

5.2 Image Resolution

Here, we explore the effects of image resolution. Specifically, we selected three resolution grid settings for the resized high-resolution image: {[4,4],[2,8],[8,2]}, {[6,4],[4,6],[3,8],[8,3]}, and {[6,8],[8,6],[4,12],[12,4]}. Table 6 presents the results. We do not observe a consistent improvement in performance with higher image resolution. A key reason is that the resolution of the most original images in these benchmarks is lower than the resolutions evaluated. Consequently, upsampling the image may degrade quality and introduce more noise. Additionally, we note that increasing the resolution may enhance commonsense reasoning capabilities (as seen in ScienceQA and MMMU), but it also tends to induce more hallucinations in the model. We plan to conduct further ablation studies on high-resolution images in the future.

6 Conclusion

We present Dragonfly, a novel LMM architecture for fine-grained understanding and reasoning within image regions. Dragonfly leverages multi-resolution visual encoding and zoom-in patch selection to focus on high-resolution image areas of images efficiently. Our results across multiple popular benchmarks underscore the effectiveness of the architecture, with Dragonfly achieving competitive performance compared to state-of-the-art LMMs in both general and biomedical tasks. The performance of Dragonfly-Medis particularly exciting, as it achieved the best-reported results for pathology QA and several medical image captioning tasks. We believe that our architecture will benefit the LMM research community, and we make our models open-source. Looking ahead, exploring more advanced visual encoders and improved selection strategies presents an exciting research opportunity. Additionally, exploring how zoom-in patch selection is integrated during the vision-language pretraining stage presents another avenue for future research. In the Appendix Section 7, we further discuss our model’s broader impact and limitations.

7 Broader Impact and Limitation

The development of Dragonfly, which focuses on fine-grained image region understanding and reasoning, has significant implications across multiple fields. The enhanced performance of Dragonfly on image understanding and reasoning tasks opens new avenues for applications in numerous domains, mainly where detailed image analysis is critical. Dragonfly finetuned on biomedical data achieves promising performance on various benchmarks, highlighting its ability to interpret accurately and reason about medical images, which can lead to improved diagnostic tools, aiding healthcare professionals in early detection and treatment planning, potentially enhancing patient outcomes, and reducing misdiagnosis. Moreover, Dragonfly can also be applied to scientific research, education, or industrial applications to benefit the broader community. Despite the decent performance, some limitations of this work should also be acknowledged. Firstly, although our architecture enhances performance in tasks requiring fine-grained details on specific image regions, it may omit some essential information for tasks that require the high-resolution details of the whole image, such as optical character recognition and chart understanding tasks. Exploring the selection ratio is one of our future research directions. Secondly, the patch selection process itself may introduce biases. While our method aims to identify the most relevant patches for specific tasks, the criteria for relevance are predefined and may not capture all important features of an image. Finally, this work only focuses on visual instruction-tuning instead of pretraining. Some claims made in this work may not apply to multimodal pretraining stages. We will explore how Dragonfly performs during multimodal pretraining in the future.

References

- AdeptAI. Fuyu-8b: A multimodal architecture for ai agents, 2023.
- Alayrac, J.-B., Donahue, J., Luc, P., Miech, A., Barr, I., Hasson, Y., Lenc, K., Mensch, A., Millican, K., Reynolds, M., et al. Flamingo: a visual language model for few-shot learning. *Advances in Neural Information Processing Systems*, 35:23716–23736, 2022.
- Awadalla, A., Gao, I., Gardner, J., Hessel, J., Hanafy, Y., Zhu, W., Marathe, K., Bitton, Y., Gadre, S., et al. Openflamingo: An open-source framework for training large autoregressive vision-language models. *arXiv preprint arXiv:2308.01390*, 2023.
- Bai, J., Bai, S., Yang, S., Wang, S., Tan, S., Wang, P., Lin, J., Zhou, C., and Zhou, J. Qwen-vl: A versatile vision-language model for understanding, localization, text reading, and beyond. *arXiv preprint arXiv:2308.12966*, 2023.
- Banerjee, S. and Lavie, A. Meteor: An automatic metric for mt evaluation with improved correlation with human judgments. In *Proceedings of the acl workshop on intrinsic and extrinsic evaluation measures for machine translation and/or summarization*, pp. 65–72, 2005.
- Chen, G. H., Chen, S., Zhang, R., Chen, J., Wu, X., Zhang, Z., Chen, Z., Li, J., Wan, X., and Wang, B. Allava: Harnessing gpt4v-synthesized data for a lite vision-language model. *arXiv preprint arXiv:2402.11684*, 2024.
- Chen, L., Li, J., Dong, X., Zhang, P., He, C., Wang, J., Zhao, F., and Lin, D. Sharegpt4v: Improving large multi-modal models with better captions. *arXiv preprint arXiv:2311.12793*, 2023a.
- Chen, L., Li, J., Dong, X., Zhang, P., He, C., Wang, J., Zhao, F., and Lin, D. Sharegpt4v: Improving large multi-modal models with better captions. *arXiv preprint arXiv:2311.12793*, 2023b.
- Dai, W., Li, J., Li, D., Tiong, A. M. H., Zhao, J., Wang, W., Li, B., Fung, P., and Hoi, S. Instruct-clip: Towards general-purpose vision-language models with instruction tuning. *arXiv preprint arXiv:2305.06500*, 2023.
- Demner-Fushman, D., Kohli, M. D., Rosenman, M. B., Shooshan, S. E., Rodriguez, L., Antani, S., Thoma, G. R., and McDonald, C. J. Preparing a collection of radiology examinations for distribution and retrieval. *Journal of the American Medical Informatics Association*, 23(2):304–310, 2016.
- Guan, T., Liu, F., Wu, X., Xian, R., Li, Z., Liu, X., Wang, X., Chen, L., Huang, F., Yacoob, Y., Manocha, D., and Zhou, T. Hallusionbench: An advanced diagnostic suite for entangled language hallucination and visual illusion in large vision-language models. *arXiv preprint arXiv:2310.14566*, 2024.
- He, X., Zhang, Y., Mou, L., Xing, E., and Xie, P. Pathvqa: 30000+ questions for medical visual question answering. *arXiv preprint arXiv:2003.10286*, 2020.
- Huang, Z., Bianchi, F., Yuksekogonul, M., Montine, T., and Zou, J. Leveraging medical twitter to build a visual-language foundation model for pathology ai. *bioRxiv*, pp. 2023–03, 2023a.
- Huang, Z., Zhang, X., and Zhang, S. Kiut: Knowledge-injected u-transformer for radiology report generation. In *Proceedings of the IEEE/CVF Conference on Computer Vision and Pattern Recognition*, pp. 19809–19818, 2023b.
- Jaegle, A., Borgeaud, S., Alayrac, J.-B., Doersch, C., Ionescu, C., Ding, D., Koppula, S., Zoran, D., Brock, A., Shelhamer, E., Hénaff, O., Botvinick, M. M., Zisserman, A., Vinyals, O., and Carreira, J. Perceiver io: A general architecture for structured inputs & outputs. *arXiv preprint arXiv:2107.14795*, 2022.
- Jing, B., Xie, P., and Xing, E. On the automatic generation of medical imaging reports. *arXiv preprint arXiv:1711.08195*, 2017.
- Johnson, A. E., Pollard, T. J., Berkowitz, S. J., Greenbaum, N. R., Lungren, M. P., Deng, C.-y., Mark, R. G., and Horng, S. Mimic-cxr, a de-identified publicly available database of chest radiographs with free-text reports. *Scientific data*, 6(1):317, 2019.

- Kembhavi, A., Salvato, M., Kolve, E., Seo, M., Hajishirzi, H., and Farhadi, A. A diagram is worth a dozen images. *arXiv preprint arXiv:1603.07396*, 2016.
- Lau, J. J., Gayen, S., Ben Abacha, A., and Demner-Fushman, D. A dataset of clinically generated visual questions and answers about radiology images. *Scientific data*, 5(1):1–10, 2018.
- Laurençon, H., Tronchon, L., Cord, M., and Sanh, V. What matters when building vision-language models? *arXiv preprint arXiv:2403.11703*, 2024.
- Li, B., Zhang, Y., Chen, L., Wang, J., Yang, J., and Liu, Z. Otter: A multi-modal model with in-context instruction tuning. *arXiv preprint arXiv:2305.03726*, 2023.
- Li, C., Wong, C., Zhang, S., Usuyama, N., Liu, H., Yang, J., Naumann, T., Poon, H., and Gao, J. Llava-med: Training a large language-and-vision assistant for biomedicine in one day. *Advances in Neural Information Processing Systems*, 36, 2024a.
- Li, L., Wang, Y., Xu, R., Wang, P., Feng, X., Kong, L., and Liu, Q. Multimodal arxiv: A dataset for improving scientific comprehension of large vision-language models. *arXiv preprint arXiv:2403.00231*, 2024b.
- Li, T., Gao, Y., Wang, K., Guo, S., Liu, H., and Kang, H. Diagnostic assessment of deep learning algorithms for diabetic retinopathy screening. *Information Sciences*, 501:511–522, 2019.
- Lin, C.-Y. Rouge: A package for automatic evaluation of summaries. In *Text summarization branches out*, pp. 74–81, 2004.
- Lin, J., Yin, H., Ping, W., Lu, Y., Molchanov, P., Tao, A., Mao, H., Kautz, J., Shoeybi, M., and Han, S. Vila: On pre-training for visual language models. *arXiv preprint arXiv:2312.07533*, 2024.
- Liu, B., Zhan, L.-M., Xu, L., Ma, L., Yang, Y., and Wu, X.-M. Slake: A semantically-labeled knowledge-enhanced dataset for medical visual question answering. In *2021 IEEE 18th International Symposium on Biomedical Imaging (ISBI)*, pp. 1650–1654. IEEE, 2021.
- Liu, H., Li, C., Li, Y., and Lee, Y. J. Improved baselines with visual instruction tuning. *arXiv preprint arXiv:2310.03744*, 2023a.
- Liu, H., Li, C., Wu, Q., and Lee, Y. J. Visual instruction tuning. *NeurIPS 2023*, 2023b.
- Liu, H., Li, C., Wu, Q., and Lee, Y. J. Visual instruction tuning. *Advances in neural information processing systems*, 36, 2024.
- Lu, P., Mishra, S., Xia, T., Qiu, L., Chang, K.-W., Zhu, S.-C., Tafjord, O., Clark, P., and Kalyan, A. Learn to explain: Multimodal reasoning via thought chains for science question answering. In *The 36th Conference on Neural Information Processing Systems (NeurIPS)*, 2022.
- Masry, A., Long, D. X., Tan, J. Q., Joty, S., and Hoque, E. Chartqa: A benchmark for question answering about charts with visual and logical reasoning. *ACL 2022 Findings*, 2022.
- McKinzie, B., Gan, Z., Fauconnier, J.-P., Dodge, S., Zhang, B., Dufter, P., Shah, D., Du, X., Peng, F., Weers, F., Belyi, A., Zhang, H., Singh, K., Kang, D., Jain, A., Hè, H., Schwarzer, M., Gunter, T., Kong, X., Zhang, A., Wang, J., Wang, C., Du, N., Lei, T., Wiseman, S., Yin, G., Lee, M., Wang, Z., Pang, R., Gräsch, P., Toshev, A., and Yang, Y. Mm1: Methods, analysis & insights from multimodal llm pre-training. *arXiv preprint arXiv:2403.09611*, 2024.
- Meta AI. Introducing meta llama 3: The most capable openly available llm to date. <https://ai.meta.com/blog/meta-llama-3/>, 2024.
- Miura, Y., Zhang, Y., Tsai, E. B., Langlotz, C. P., and Jurafsky, D. Improving factual completeness and consistency of image-to-text radiology report generation. *arXiv preprint arXiv:2010.10042*, 2020.
- Moor, M., Huang, Q., Wu, S., Yasunaga, M., Dalmia, Y., Leskovec, J., Zakka, C., Reis, E. P., and Rajpurkar, P. Med-flamingo: a multimodal medical few-shot learner. In *Machine Learning for Health (ML4H)*, pp. 353–367. PMLR, 2023.

- Pelka, O., Koitka, S., Rückert, J., Nensa, F., and Friedrich, C. M. Radiology objects in context (roco): a multimodal image dataset. In *Intravascular Imaging and Computer Assisted Stenting and Large-Scale Annotation of Biomedical Data and Expert Label Synthesis: 7th Joint International Workshop, CVII-STENT 2018 and Third International Workshop, LABELS 2018, Held in Conjunction with MICCAI 2018, Granada, Spain, September 16, 2018, Proceedings 3*, pp. 180–189. Springer, 2018.
- Radford, A., Kim, J. W., Hallacy, C., Ramesh, A., Goh, G., Agarwal, S., Sastry, G., Askell, A., Mishkin, P., Clark, J., et al. Learning transferable visual models from natural language supervision. In *International conference on machine learning*, pp. 8748–8763. PMLR, 2021.
- Saab, K., Tu, T., Weng, W.-H., Tanno, R., Stutz, D., Wulczyn, E., Zhang, F., Strother, T., Park, C., Vedadi, E., et al. Capabilities of gemini models in medicine. *arXiv preprint arXiv:2404.18416*, 2024.
- Subramanian, S., Wang, L. L., Mehta, S., Bogin, B., van Zuylen, M., Parasa, S., Singh, S., Gardner, M., and Hajishirzi, H. Medcat: A dataset of medical images, captions, and textual references. *arXiv preprint arXiv:2010.06000*, 2020.
- Tanwani, A. K., Barral, J., and Freedman, D. Reptsnet: Combining vision with language for automated medical reports. In *International Conference on Medical Image Computing and Computer-Assisted Intervention*, pp. 714–724. Springer, 2022.
- Tsung-Yi, L., Michael, M., Serge, B., Lubomir, B., Ross, G., James, H., Pietro, P., Deva, R., C. Lawrence, Z., and Piotr, D. Microsoft coco: Common objects in context. *arXiv preprint arXiv:1405.0312*, 2015.
- Tu, T., Azizi, S., Driess, D., Schaekermann, M., Amin, M., Chang, P.-C., Carroll, A., Lau, C., Tanno, R., Ktena, I., et al. Towards generalist biomedical ai. *NEJM AI*, 1(3):AIoa2300138, 2024.
- Vedantam, R., Lawrence Zitnick, C., and Parikh, D. Cider: Consensus-based image description evaluation. In *Proceedings of the IEEE conference on computer vision and pattern recognition*, pp. 4566–4575, 2015.
- Wang, Z., Liu, L., Wang, L., and Zhou, L. Metransformer: Radiology report generation by transformer with multiple learnable expert tokens. In *Proceedings of the IEEE/CVF Conference on Computer Vision and Pattern Recognition (CVPR)*, pp. 11558–11567, June 2023.
- Wei, J., Tay, Y., Bommasani, R., Raffel, C., Zoph, B., Borgeaud, S., Yogatama, D., Bosma, M., Zhou, D., Metzler, D., et al. Emergent abilities of large language models. *arXiv preprint arXiv:2206.07682*, 2022.
- Weihao, Y., Zhengyuan, Y., Linjie, L., Jianfeng, W., Kevin, L., Zicheng, L., Xinchao, W., and Lijuan, W. Mm-vet: Evaluating large multimodal models for integrated capabilities. *arXiv preprint arXiv:2308.02490*, 2023.
- Xiang, Y., Yuansheng, N., Kai, Z., Tianyu, Z., Ruoqi, L., Ge, Z., Samuel, S., Dongfu, J., Weiming, R., Yuxuan, S., Cong, W., Botao, Y., Ruibin, Y., Renliang, S., Ming, Y., Boyuan, Z., Zhenzhu, Y., Yibo, L., Wenhao, H., Huan, S., Yu, S., and Wenhao, C. Mmmu: A massive multi-discipline multimodal understanding and reasoning benchmark for expert agi. *arXiv preprint arXiv:2311.16502*, 2023.
- Xu, R., Yao, Y., Guo, Z., Cui, J., Ni, Z., Ge, C., Chua, T.-S., Liu, Z., Sun, M., and Huang, G. Llava-uhd: an lmm perceiving any aspect ratio and high-resolution images. *arXiv preprint arXiv:2403.11703*, 2023.
- Yang, Z., Li, L., Wang, J., Lin, K., Azarnasab, E., Ahmed, F., Liu, Z., Liu, C., Zeng, M., and Wang, L. Mm-react: Prompting chatgpt for multimodal reasoning and action. *arXiv preprint arXiv:2303.11381*, 2023.
- Yifan, L., Yifan, D., Kun, Z., Jinpeng, W., Wayne, X. Z., and Ji-Rong, W. Evaluating object hallucination in large vision-language models. In *The 2023 Conference on Empirical Methods in Natural Language Processing*, 2023. URL <https://openreview.net/forum?id=xozJw0kZXF>.
- You, H., Zhang, H., Gan, Z., Du, X., Zhang, B., Wang, Z., Cao, L., Chang, S.-F., and Yang, Y. Ferret: Refer and ground anything anywhere at any granularity. *arXiv preprint arXiv:2310.07704*, 2023.

- Yuan, Z., Jin, Q., Tan, C., Zhao, Z., Yuan, H., Huang, F., and Huang, S. Ramm: Retrieval-augmented biomedical visual question answering with multi-modal pre-training. In *Proceedings of the 31st ACM International Conference on Multimedia*, pp. 547–556, 2023.
- Zhang, H., You, H., Dufter, P., Zhang, B., Chen, C., Chen, H.-Y., Fu, T.-J., Wang, W. Y., Chang, S.-F., Gan, Z., and Yang, Y. Ferret-v2: An improved baseline for referring and grounding with large language models. *arXiv preprint arXiv:2403.11703*, 2024.
- Zhang, K., Yu, J., Yan, Z., Liu, Y., Adhikarla, E., Fu, S., Chen, X., Chen, C., Zhou, Y., Li, X., et al. Biomedgpt: A unified and generalist biomedical generative pre-trained transformer for vision, language, and multimodal tasks. *arXiv preprint arXiv:2305.17100*, 2023a.
- Zhang, S., Xu, Y., Usuyama, N., Xu, H., Bagga, J., Tinn, R., Preston, S., Rao, R., Wei, M., Valluri, N., et al. Biomedclip: a multimodal biomedical foundation model pretrained from fifteen million scientific image-text pairs. *arXiv preprint arXiv:2303.00915*, 2023b.
- Zhao, B., Wu, B., He, M., and Huang, T. Svit: Scaling up visual instruction tuning. *arXiv preprint arXiv:2307.04087*, 2023a.
- Zhao, B., Wu, B., and Huang, T. Svit: Scaling up visual instruction tuning. *arXiv preprint arXiv:2307.04087*, 2023b.
- Zhou, Y., Huang, L., Zhou, T., Fu, H., and Shao, L. Visual-textual attentive semantic consistency for medical report generation. In *Proceedings of the IEEE/CVF International Conference on Computer Vision*, pp. 3985–3994, 2021.

Supplementary Material

A General Training Data Description

We collected and curated a vision instruction tuning dataset from ShareGPT4V (Chen et al., 2023b), ALLaVA (Chen et al., 2024), SVIT (Zhao et al., 2023a), and a subset tasks from the Cauldron (Laurençon et al., 2024). We initially combined all the samples from these four resources, resulting in nearly 9 million samples. During experiments on the training data, we have several lessons:

- Increasing the number of training samples during the visual instruction tuning improves the accuracy of commonsense reasoning tasks but also introduces more hallucination. To reduce hallucinations, the model should be trained on specialized data.
- Deduplicating the training samples is important. Duplicated samples may introduce additional bias during the training.
- Question-answering data can improve the performance on benchmarks but reduce the details and length of the generated text

Based on the lessons learned, we first deduplicate the image and instruction pairs. SVIT and ShreGPT4V share the same image set, and to scale up the samples, SVIT generates multiple instructions for each image. Therefore, for each image, we only randomly pick eight instructions. The Cauldron dataset is a massive collection of 50 high-quality datasets converted to the user/assistant format. However, some of the datasets include math or coding. We observe some misalignment during the training if we include these datasets. Thus, we remove five datasets from the Cauldron dataset. After the processing and deduplication, our final training set has 5,580,560 image-instruction pairs. Besides the image-instruction pairs, we also add text-only data to keep the zero-shot capability of the model. We use the data from OpenHermes and MathInstruct.

B General Benchmarks

Here, we introduce the evaluation benchmarks we used in our experiments.

AI2D AI2D dataset (Kembhavi et al., 2016) is a dataset of illustrative diagrams for research on diagram understanding and associated question answering. The dataset covers over 5,000 grade school science diagrams with over 150,000 rich annotations. We use the test split of AI2D dataset, which contains 3,088 samples.

ScienceQA ScienceQA dataset (Lu et al., 2022) aims to evaluate the multimodal commonsense reasoning capabilities of the models and is collected from elementary and high school science curricula, and contains 21,208 multimodal multiple-choice science questions. This dataset has richer domain diversity from three subjects: natural science, language science, and social science. In this paper, we use the popular evaluation split with 4,114 samples.

ChartQA ChartQA dataset (Masry et al., 2022) is a benchmark for question answering about charts with visual and logical reasoning. This dataset requires the model to have understanding and reasoning capabilities across the information of the whole image. We use the test split with 2,500 samples to evaluate our model.

MMMU Massive Multi-discipline Multimodal Understanding and Reasoning benchmark (MMMU) (Xiang et al., 2023) is a benchmark to access the expert-level multimodal understanding capability of foundation models across a broad scope of tasks. The dataset covers subjects and disciplines including Art, Business, Health & Medicine, Science, Humanities & Social Science, and Tech & Engineering and over subfields. This benchmark measures three essential skills in LMMs: perception, knowledge, and reasoning. Dragonfly performs competitively on this benchmark, providing evidence of strong multimodal capabilities.

MMVet MMVet dataset (Weihao et al., 2023) is an evaluation benchmark that examines LMMs on complicated multimodal tasks. MMVet defines six core vision-language capabilities and examines

the 16 integrations of interest derived from the capability combination. This dataset uses GPT4 to evaluate the generated open-ended outputs and provides a unified scoring metric.

POPE POPE dataset (Yifan et al., 2023) aims to evaluate the object hallucination of LMMs using a polling-based query method. This dataset is widely used to assess object hallucination more stably and flexibly. We use the test split of this dataset with 9,000 samples and the F1 score as the evaluation metric.

COCO Caption COCO dataset (Tsung-Yi et al., 2015) is a large-scale object detection, segmentation, key-point detection, and captioning dataset. The dataset consists of 328K images. This dataset has multiple tasks, including captioning, question-answering, object detection, and segmentation. We use the COCO-2017 validation set to evaluate the model’s captioning capability.

Hallucination-Bench Hallucination-Bench (Guan et al., 2024) is a comprehensive benchmark designed to evaluate image-context reasoning. It emphasizes nuanced understanding and interpretation of visual data, which presents significant challenges to advanced LMMS. This benchmark uses the GPT4 to compute a unified evaluation score.

C Biomedical Training Data Description

Many public datasets were used in the training and evaluation of Dragonfly. All datasets were de-identified. Open datasets were used following their existing licenses.

C.1 LLaVA-Med

LLaVA-Med is a dataset for instruction-following tasks involving multi-round conversations about biomedical images, generated using the language-only model GPT-4 (Li et al. (2024a)). Specifically, the model is prompted to generate questions and answers in multi-round formats based on an image caption, as if it could view the image itself. To assemble the image captions and their contexts, LLaVA-Med utilizes PMC-15M (Zhang et al. (2023b)) to select images that contain a single plot. From these, it samples 60,000 image-text pairs from the five most prevalent imaging modalities: CXR (chest X-ray), CT (computed tomography), MRI (magnetic resonance imaging), histopathology, and gross pathology. The dataset also extracts sentences referencing the image from the original PubMed articles to provide additional context to the captions. LLaVA-Med offers two primary versions of the dataset: (i) 60K-IM, which includes inline mentions as context, and (ii) 60K, a similar-sized dataset that excludes inline mentions in its self-instruct generations. Furthermore, a supplementary dataset of 500,000 image-caption pairs is available for alignment purposes. Data link: <https://github.com/microsoft/LLaVA-Med>

C.2 Medicat

Medicat (Subramanian et al. (2020)) is a dataset of medical figures, captions, subfigures/subcaptions, and inline references that enables the study of these figures in context. It consists of 217,000 images from 131,000 open-access PubMed Central and includes captions, inline references for 74% of figures, and manually annotated subfigures and subcaptions for a subset of figures. Data link: <https://github.com/allenai/medicat>.

C.3 MIMIC-III-CXR

The MIMIC-III-CXR dataset (Johnson et al. (2019)) is a substantial publicly available collection of chest radiographs, containing 377,110 images derived from 227,827 imaging studies conducted at the Beth Israel Deaconess Medical Center from 2011 to 2016. Each image in the dataset is paired with structured labels extracted from free-text radiology reports. The dataset is organized into training, validation, and testing subsets, with 368,960 images allocated for training, 2,991 for validation, and 5,159 for testing. To ensure patient confidentiality, all images have been de-identified. Data link: <https://physionet.org/content/mimic-cxr-jpg/2.1.0/>

C.4 Openpath

OpenPath dataset is an expansive collection of 208,414 pathology image-text pairs, making it the largest publicly available pathology image dataset annotated with text descriptions (Huang et al. (2023a)). This dataset was meticulously curated using popular pathology-related hashtags recommended by the United States and Canadian Academy for Pathology (USCAP) and the Pathology Hashtag Ontology projects. It spans images gathered from Twitter and other internet sites, including the LAION dataset, collected between March 21, 2006, and November 15, 2022. The dataset consists of three main components: (1) Tweets, with 116,504 image-text pairs; (2) Replies, comprising 59,869 pairs from highly liked responses; and (3) PathLAION, which adds 32,041 pairs from broader internet sources. Data link: <https://github.com/PathologyFoundation/plip>.

C.5 Kaggle DR (Diabetic Retinopathy)

The Kaggle website organized a DR detection challenge in 2015 Li et al. (2019). The California Healthcare Foundation sponsored the competition. The Kaggle DR dataset consists of 88,702 color fundus images, including 35,126 samples for training and 53,576 samples for testing. Different devices captured the images under various conditions (e.g., resolutions) at multiple primary care sites throughout California and elsewhere. For each subject, two images of the left and right eyes were collected with the same resolution. Clinicians rate each image for the presence of DR on a scale of 0–4 according to the ETDRS scale. Data link: <https://www.kaggle.com/c/diabetic-retinopathy-detection>.

C.6 DDR

DDR is a diabetic retinopathy dataset (Li et al. (2019)) that comprises 13,673 color fundus images collected from 147 hospitals across 23 provinces in China between 2016 and 2018, ensuring a broad demographic spread by including images from patients aged 1 to 100, averaging 54.13 years, and almost evenly split between males (48.23%) and females (51.77%). These images, derived from 9,598 patients and captured using 42 types of fundus cameras, adhere to stringent photographic standards to ensure clarity and appropriate exposure, focusing on crucial retinal structures and lesions. All images have been desensitized for widespread usage and graded for diabetic retinopathy (DR) severity by seven trained graders using the International Classification of Diabetic Retinopathy, supplemented by consensus and consultation with experienced specialists where necessary. Data link: <https://github.com/nkicssl/DDR-dataset>.

C.7 ROCO

The Radiology Objects in Context (ROCO) dataset is a comprehensive collection of over 81,000 radiology images derived from PubMedCentral’s open-access biomedical literature (Pelka et al. (2018)). The dataset focuses on analyzing visual elements and semantic relationships within radiological imagery. It includes a variety of medical imaging modalities such as Computer Tomography (CT), Ultrasound, X-ray, Fluoroscopy, Positron Emission Tomography (PET), Mammography, Magnetic Resonance Imaging (MRI), and Angiography. Each image is accompanied by detailed metadata, including captions, keywords, and identifiers from the Unified Medical Language System (UMLS). The ROCO dataset also features an out-of-class set of approximately 6,000 images, ranging from synthetic radiology figures to digital art, to aid in improving prediction and classification tasks. The dataset is split into training, validation, and test sets with 70,308, 8,782, and 8,786 images, respectively.

C.8 VQA-RAD

The VQA-RAD dataset (Lau et al. (2018)) contains 314 radiology images and 2,244 question-answer pairs obtained from CT, MRI, and X-ray examinations, covering three anatomical regions: the head, abdomen, and chest. It features a diverse range of question styles, categorized into 11 types: modality, plane, organ system, abnormalities, etc. Among these, 58% of the question-answer pairs are closed-ended (yes/no), with the remaining 42% being open-ended. The dataset is segmented into a training set of 1,790 QA pairs and a testing set of 451 QA pairs. Our model

was trained on the official training set and evaluated on the official test set. Data link: <https://huggingface.co/datasets/flaviagammarino/vqa-rad>.

C.9 SLAKE

The Slake-VQA dataset, annotated by expert physicians (Liu et al. (2021)), is a comprehensive bilingual (English and Chinese) VQA dataset. It includes 642 images and 14,028 question-answer pairs across three imaging modalities: CXR, CT, and MRI. This dataset spans various radiological areas, covering body regions such as the brain, neck, chest, abdomen, and pelvic cavity. It contains 9,849 VQA samples designated for training, 2,109 for validation, and 2,070 for testing. The questions vary widely, featuring both open-ended (free-form) and closed-ended (yes/no) types that assess different image characteristics like plane, quality, position, organ, abnormality, size, color, shape, and pertinent medical knowledge. We utilized only the English-language examples from the official dataset divisions, comprising 4,919 training, 1,053 validation, and 1,061 test examples. Our model was trained on the official training set and evaluated on the official test set. Data link: <https://www.med-vqa.com/slake/>

C.10 Path-VQA

This dataset comprises question-answer pairs relating to pathology images (He et al. (2020)). It encompasses a variety of question formats, including open-ended and closed-ended (yes/no) questions. The dataset is constructed through automated techniques and draws from two open-access pathology textbooks and a digital library. It encompasses a total of 32,632 question-answer pairs derived from 4,289 images. The dataset is partitioned into official training, validation, and test subsets, containing 19,654, 6,259, and 6,719 QA pairs, respectively. Our model was trained on the official training set and evaluated on the official test set. Data link: <https://github.com/UCSD-AI4H/PathVQA/tree/master/data>

C.11 IU X-ray

The IU X-ray dataset, detailed in Demner-Fushman et al. (2016), is available through the Open Access Biomedical Image Search Engine (OpenI). This collection includes radiological exams or cases, each associated with one or more images, a radiology report, and two sets of tags. The reports consist of four sections: Comparison, Indication, Findings, and Impression, with the latter two sections useful for image captioning. The dataset features two types of tags: MTI tags derived automatically from the report text by the Medical Text Indexer and manual tags assigned by two trained coders. Overall, it comprises 3,955 reports and 7,470 frontal and lateral X-ray images. The dataset is divided into 6,698 samples in the training set and 745 samples in the test set. Data link: <https://github.com/nlpaueb/bioCaption>

C.12 Peir Gross

The Peir Gross dataset, initially utilized for captioning in research by Jing et al. (2017), features photographs from medical cases sourced from the Pathology Education Informational Resource (PEIR) digital library intended for educational purposes in pathology. This dataset includes 7,443 images from the Gross collections across 21 pathology sub-categories in PEIR, with each image paired with a descriptive single-sentence caption. It is organized into two subsets: 5,172 images for training and 1,289 for testing. Data link: <https://github.com/nlpaueb/bioCaption>

D Biomedical Benchmarks

The details of our evaluation benchmarks are discussed in Section C. A benchmark summary table is also included in 7.

Table 7: Summary of the biomedical evaluation benchmark, which includes vision question answering, image captioning, and report generation across radiology and pathology modalities. We finetuned the model using a subset of the official training set and evaluated it on the official testing set. It should be noted that for MIMIC-CXR and ROCO, we utilized only a portion of the training dataset. Furthermore, for MIMIC-CXR, we selected only those subsets of the test set, including a findings section.

Task Type	Modality	Dataset	Split	
			Train	Test
Visual Question Answering	Radiology	VQA-RAD	1,790	451
	Radiology	Slake-VQA	4,919	1,053
	Pathology	Path-VQA	19,654	6,719
Report Generation	Chest X-ray	MIMIC-CXR	25,000	3,513
Image Captioning	Radiology	ROCO	25,000	8,786
	Radiology	IU X-RAY	6,698	745
	Pathology	Peir Gross	5,172	1,289